

Article

Construction of a ZnO Heterogeneous Structure Using Co₃O₄ as a Co-Catalyst to Enhance Photoelectrochemical Performance

Aiymkul A. Markhabayeva ^{*}, Zhanar K. Kalkozova , Renata Nemkayeva , Yerassyl Yerlanuly ,
Assiya S. Anarova, Malika A. Tulegenova, Aida T. Tulegenova  and Khabibulla A. Abdullin 

Faculty of Physics and Technology, Al Farabi Kazakh National University, 71 Al-Farabi Avenue, Almaty 050040, Kazakhstan; zh.kalkozova@mail.ru (Z.K.K.); quasisensus@mail.ru (R.N.); yerlanuly@physics.kz (Y.Y.); assiya.anarova@gmail.com (A.S.A.); malika.tulegenova@bk.ru (M.A.T.); tulegenova.aida@gmail.com (A.T.T.); kh.abdullin@physics.kz (K.A.A.)

* Correspondence: aiko_marx@mail.ru

Abstract: Recently, heterostructured photocatalysts have gained significant attention in the field of photocatalysis due to their superior properties compared to single photocatalysts. One of the key advantages of heterostructured photocatalysts is their ability to enhance charge separation and broaden the absorption spectrum, thereby improving photocatalytic efficiency. Zinc oxide is a widely used n-type semiconductor with a proper photoelectrochemical activity. In this study, zinc oxide nanorod arrays were synthesized, and then the surfaces of ZnO nanorods were modified with the p-type semiconductor Co₃O₄ to create a p–n junction heterostructure. A significant increase in the photocurrent for the ZnO/Co₃O₄ composite, of 4.3 times, was found compared to pure ZnO. The dependence of the photocurrent on the morphology of the ZnO/Co₃O₄ composite allows for optimization of the morphology of the ZnO nanorod array to achieve improved photoelectrochemical performance. The results showed that the ZnO/Co₃O₄ heterostructure exhibited a photocurrent density of 3.46 mA/cm², while bare ZnO demonstrated a photocurrent density of 0.8 mA/cm² at 1.23 V. The results of this study provide a better understanding of the mechanism of charge separation and transfer in the heterostructural ZnO/Co₃O₄ photocatalytic system. Furthermore, the results will be useful for the design and optimization of photocatalytic systems for water splitting and other applications.

Keywords: photocatalyst; heterogeneous; nanorods; photoelectrochemical water splitting



Citation: Markhabayeva, A.A.; Kalkozova, Z.K.; Nemkayeva, R.; Yerlanuly, Y.; Anarova, A.S.; Tulegenova, M.A.; Tulegenova, A.T.; Abdullin, K.A. Construction of a ZnO Heterogeneous Structure Using Co₃O₄ as a Co-Catalyst to Enhance Photoelectrochemical Performance. *Materials* **2024**, *17*, 146. <https://doi.org/10.3390/ma17010146>

Academic Editors: Barbara Pawelec and Alexey N. Pstryakov

Received: 2 November 2023

Revised: 15 December 2023

Accepted: 19 December 2023

Published: 27 December 2023



Copyright: © 2023 by the authors. Licensee MDPI, Basel, Switzerland. This article is an open access article distributed under the terms and conditions of the Creative Commons Attribution (CC BY) license (<https://creativecommons.org/licenses/by/4.0/>).

1. Introduction

In recent years, there has been a growing interest in alternative energy sources to compensate for diminishing fossil fuel resources. Harnessing solar energy is a promising way to counteract the energy crisis [1]. Efficient photoelectrochemical (PEC) water splitting systems offer a potential solution for the conversion of solar energy into other forms of energy. Effective water splitting technology requires a high light absorption coefficient and stable photocatalysts with appropriate bandgap energy. The energy levels of the conduction band (CB) in semiconductors need to be situated at a lower value than the hydrogen reduction potential (0 V vs. NHE), whereas the valence band (VB) should be at a higher energy level than the oxidation potential of oxygen (1.23 V vs. NHE). However, many metal oxide semiconductors that can absorb visible light and have a narrow bandgap of less than 2 eV do not have suitable VB and CB positions for water splitting. To overcome this, various techniques have been employed, such as doping with extraneous atoms to increase the number of states near the CB or VB, altering the particle size, using combinations of materials for efficient energy or electron transfer to absorb light with different energies, or employing plasmonic excitation to enhance the light absorption and photocatalytic efficiency [2–5].

Among the metal oxides, ZnO, TiO₂ [6,7], and ZrO₂ exhibit both conduction and valence band energies suitable for water splitting [8,9]. In particular, ZnO is an n-type direct-gap semiconductor with a band gap of ~3.3 eV at room temperature. The value of optical transmission is 85–90% in the range of 400–700 nm for ZnO thin films [10,11]. Due to its low toxicity and high electronic conductivity, it has been extensively studied for various optoelectronic applications [12], including solar cells, gas sensors, and phosphors. In addition, ZnO exhibits better light absorption than TiO₂, because its refractive index is lower (2.0) than that of TiO₂ (2.5–2.7), resulting in increased transparency and reduced light scattering.

However, zinc oxide is susceptible to photocorrosion in aqueous and acidic electrolytes and dissolves to form Zn(OH)₂ [13]. Despite this limitation, experimental results have shown that ZnO actually exhibits higher photocatalytic activity than TiO₂ and other semiconductor catalysts, such as CdS, WO₃, Fe₂O₃, SnO₂, ZrO₂, and GaSe [14], especially in the degradation of dyes in aqueous solution [15–19]. These advantages make it a good candidate for a photoelectrode in photoelectrochemical cells for water oxidation.

Significant research efforts have been dedicated to the exploration of ZnO nanorod arrays, leading to the development of diverse device structures. This is evident in various reviews [20–22]. The appeal of such arrays lies in their facile synthesis, high crystallinity, excellent electrical properties, and substantial specific area. Noteworthy studies in related areas include an examination of morphological changes in a ZnO nanorod array with cobalt oxide particles, both pre- and post-photoelectrochemical (PEC) measurements [23]. Additionally, research, such as [24], has delved into variations in photoelectric properties in Co₃O₄/ZnO samples with different concentrations of the cobalt precursor. Another study, [25], focused on synthesizing ZnO/Co₃O₄ nanoparticles with varying cobalt contents. Considering these factors, the investigation of the photocatalytic properties of ZnO/Co₃O₄ structures for water decomposition emerges as a highly relevant and unexplored avenue in the existing body of literature.

The combination of ZnO with Co₃O₄, a p-type semiconductor with a band gap of 2.1 eV and known surface catalytic activity, showed improved photoelectrochemical performance [26] and oxygen evolution reaction [27], by separating charge carriers at the p–n interface [28,29]. Based on our previous experience [30], the formation of a WO₃/Co₃O₄ p–n type heterojunction reduced the recombination of photocatalytic charges and enhanced the light absorption capabilities, resulting in a photocurrent 20 times higher than that of pristine WO₃.

In this study, we synthesized a photocatalytic composite consisting of a ZnO nanorod array and a Co₃O₄ nanoparticle cocatalyst. A significant finding revealed a fourfold enhancement in the photocurrent within the ZnO/Co₃O₄ system when compared to ZnO alone. Furthermore, the photocurrent's correlation with the size of ZnO nanorods exhibits a non-monotonic pattern, suggesting the potential for maximizing photocurrent and optimizing photocatalytic properties in the ZnO/Co₃O₄ system by tailoring the morphology of ZnO nanorod arrays.

2. Experimental Sections

2.1. Chemicals

Zinc acetate dehydrate (99.99%), zinc nitrate hexahydrate (98%), urotropine (99%), cobalt nitrate hexahydrate (99%), sodium sulfide (95%), and hexamethylenetetramine C₆H₁₂N₄ (99%) were purchased from Sigma Aldrich (St. Louis, MO, USA). High purity water (18.2 MΩ·cm) was supplied via the ARIUM 611 DI water purification system, Sartorius Group (Göttingen, Germany). All reagents were used without purification.

2.2. Synthesis

2.2.1. Spin Coating Technique for Deposition of ZnO Seed Layer

In the initial step, a spin coating technique was employed to deposit thin zinc oxide seed layers on the ITO substrates. Prior to synthesis, glass substrates coated with indium

tin oxide (ITO) (resistivity of 10 Ω /cm) were thoroughly cleaned in a washing solution consisting of H₂O:H₂O₂:NH₄OH in a ratio of 4:1:1.

The sol was prepared by dissolving 0.4 g of zinc acetate Zn(CH₃COO)₂ in 10 mL of ethanol (96%) at room temperature. To ensure a clear solution, a few drops of lactic acid C₃H₆O₃ (80%) were added to prevent aggregation. The resulting clear solution was then applied to the surface of the ITO substrate through centrifugation at 1000 rpm for 5 min.

Subsequently, the substrates were then dried at 100 °C for 15 min. A final annealing step was performed at 300 °C for 60 min in a muffle furnace. As a result, thin and transparent ZnO layers were formed on the ITO substrates.

2.2.2. Chemical Bath Deposition of ZnO

ZnO nanorods were synthesized via chemical bath deposition. The second stage of the synthesis was the growth of ZnO nanorods. For this purpose, the substrates coated with seed layers were carefully placed into a beaker containing a solution composed of zinc nitrate, Zn(NO₃)₂, and hexamethylenetetramine, C₆H₁₂N₄. The concentration of the solution was systematically varied at 25, 50, and 75 mM.

The beaker was then placed in a water bath and heated to a constant temperature of 90 °C. The reaction was allowed to proceed for 1 h. The substrates were then extracted from the solution, washed with distilled water, and dried at 100 °C. As a result of these procedures, ZnO nanorods were formed on the surface of the ITO substrate, demonstrating the successful outcome of this synthesis process.

2.2.3. Deposition of Cobalt Oxide on the Surface of Zinc Oxide

A spin coating technique was further applied to deposit the cobalt oxide layer on top of the prepared ZnO nanorods. For sol preparation, cobalt nitrate, Co(NO₃)₂, was dissolved in 10 mL of ethanol at room temperature. ZnO photoelectrodes were fixed on a rotating disk, and then an alcoholic solution of cobalt nitrate was dropped onto the ZnO surface. The concentration of the cobalt solution was 0.007 M. The rotation speed was 1000 revolutions per minute (rpm) so that the solution completely covered the surface. The procedure was repeated three times, after which the samples were dried and then annealed at a temperature of 350 °C for 1 h in air. The rate of temperature increase during the heat treatment was 5 °C per minute.

3. Material Characterization

The film morphology was studied using scanning electron microscopy (SEM) on a Quanta 3D 200i microscope (FEI, Brno, Czech Republic) equipped with an energy dispersive X-ray spectroscopy (EDX) system. The crystal structure of the films was studied using a MiniFlex X-ray diffractometer (Rigaku, Tokyo, Japan). The XPS spectra were obtained using an X-ray photoelectron spectrometer (NEXSA, Thermo Scientific, Waltham, MA, USA). Raman spectra were obtained using a Ntegra Spectra (Solver Spectrum, NT-MDT Co., Ltd., Zelenograd, Russia) spectrometer with 473 nm excitation. Photocurrent measurements were performed using a xenon solar simulator (PLS-SXE300, Perfect light, China) with a 1.5 AM filter and a Corrtest CS310 potentiostat (Corrtest Instruments, China).

4. Photoelectrochemical Measurements

Photoelectrochemical (PEC) measurements including linear sweep voltammetry (LSV) and electrochemical impedance spectroscopy (EIS) were carried out to study the PEC material. Photocurrent measurements were performed using a Xenon solar lamp (AM 1.5 G, 100 mW/cm²), potentiostat, and a quartz cell. All photoelectrochemical and deposition experiments were carried out at room temperature using a standard three-electrode system with a Pt counter electrode and an Ag/AgCl reference electrode. The area of the working photoelectrode was 1 cm², and the rest of the electrode was covered with epoxy resin. An aqueous solution of electrolyte containing Na₂S (0.5 M) and Na₂SO₃ (0.5 M) was used as the electrolyte. The Nernst equation is used to convert poten-

tials: $V_{RHE} = V_{Ag/AgCl} + 0.0591 \times \text{pH} + V_{Ag/AgCl}^0$, where $V_{Ag/AgCl}$ is the applied potential, $V_{Ag/AgCl}^0$ is the standard potential of the Ag/AgCl reference electrode, and pH is basicity or acidity of the electrolyte. The pH of the electrolyte was 8.4. The sample was illuminated from the reverse side of the working electrode. The scan rate of the LSV under dark and light illumination was 10 mV/s.

5. Results and Discussion

Figure 1 illustrates the morphology of the samples obtained in this study. It can be seen (Figure 1) that the ZnO nanorods have a hexagonal shape and are predominantly located perpendicular to the substrate, and the ZnO (002) reflection in Figure 2 has the maximum intensity and corresponds to the preferential growth of nanorods; therefore, nanorods are single crystals. The surface of the ZnO nanorods (Figure 1a) is smooth; the surface becomes rough after cobalt deposition (Figure 1b). It is seen that the diameter and the length of nanorods is changed after cobalt deposition. Nevertheless, the Co_3O_4 layer exhibits uniform growth over ZnO nanostructures, forming an interconnected network of ultrathin Co_3O_4 that links all the ZnO nanostructures.

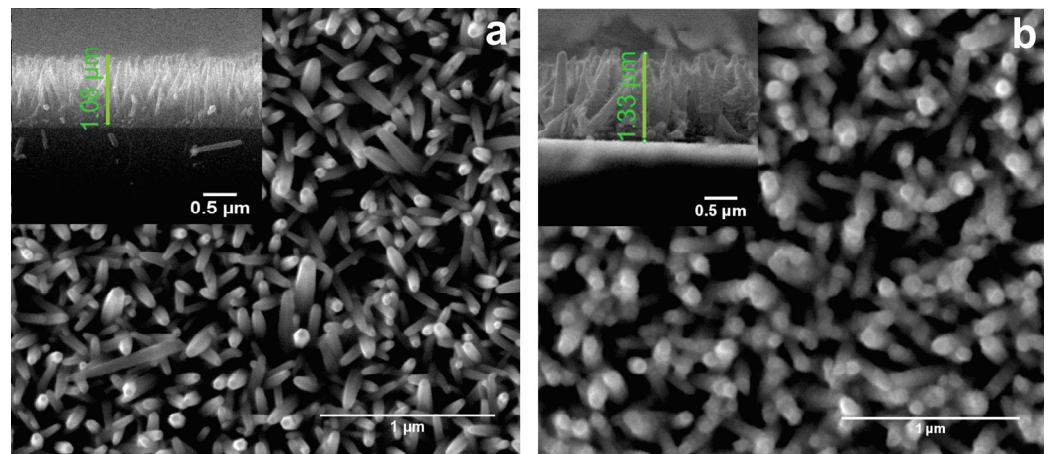


Figure 1. SEM images of ZnO nanorods grown from a solution with a zinc concentration of (a) 50 mM, (b) after cobalt deposition, and inset is cross-section images, respectively.

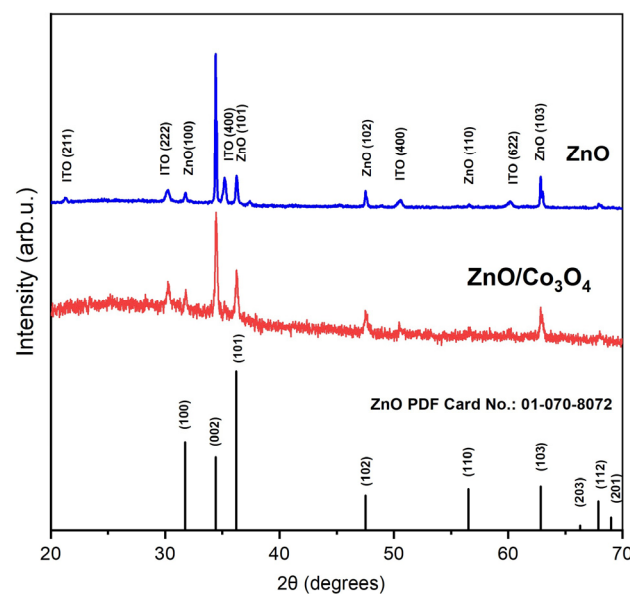
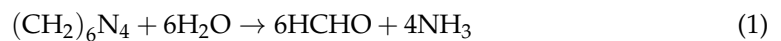


Figure 2. XRD patterns of ZnO and ZnO/ Co_3O_4 on an ITO substrate.

The diameter of the rods synthesized at different concentrations of zinc solution shows minimal variation (Figure S1). By examining the cross-sectional image, we can determine the length of these rods. The length of the nanorods and their diameter can be varied depending on the concentration of precursors in the growth solution at a fixed synthesis time. At a concentration of 25 mM, the rods have lateral length of approximately 530 nm (Figure S1a). At 50 mM, the lateral length increases to $\sim 1 \mu\text{m}$ (Figure S1b). Finally, at 75 mM, the lateral length reaches $\sim 1.5 \mu\text{m}$ (Figure S1c). These findings indicate that with increasing concentration, the diameters of the rods show minimal change, while the length of the rods increases significantly.

The following are the commonly referenced overall reactions in the literature for the synthesis of ZnO using zinc nitrate and hexamethylenetetramine (HMTA) precursors, as documented in references [31–33]:



When HMTA is heated, it decomposes into ammonia and formaldehyde as shown in Equation (1). Subsequently, the ammonia reacts with water to generate hydroxide ions OH^- (as depicted in Equation (2)), these hydroxide ions play a vital role in the crystallization of ZnO (Equations (3) and (4)). The concentration of precursors in a solution is a key factor in the growth process, as it directly influences the size of the resulting crystals. In the case of ZnO nanorods, the size-dependent properties of these structures have garnered significant attention due to their relevance in various applications [34–36]. For example, Lestari et al. showed that the structural and optical properties of ZnO nanorods varied with precursor concentration (0.002, 0.06, and 0.1 M) [37]. Horachit et al. fabricated a perovskite solar cell using ZnO nanorods, and the concentration of precursor solution (100 mM) affected the size and density of the nanorods, resulting in a 2.26% conversion efficiency [38]. Based on these findings, we selected precursor concentrations of 25, 50, and 75 mM to synthesize ZnO nanorods to study their impact on the photoelectrochemical properties.

X-ray diffraction studies of ZnO nanorods are shown in Figure 2. The peaks at angles of 21.2° , 30.2° , 35.15° , 50.6° , and 60.1° correspond to the ITO glass substrate. The diffraction peaks at 31.8° , 34.4° , 36.3° , 47.4° , 56.6° , and 62.8° can be indexed to the hexagonal phase of ZnO (PDF#01-0708072). A stronger peak intensity at the (002) plane compared to other peaks indicates the preferential growth of nanorods in the (002) direction. No significant changes were found in the XRD analysis after modification of ZnO with Co nitrate solution. This is explained by the low concentration of cobalt precursor in the heterojunction nanomaterial.

Raman spectroscopy was used to confirm the presence of cobalt oxide on top of zinc oxide. The Raman spectrum of the initial ZnO depicted in Figure 3a demonstrates the main typical bands at 99, 437, and 580 cm^{-1} assigned to E_2 (low), E_2 (high), and $A_1(\text{LO})/E_1(\text{LO})$ phonon modes, respectively [39,40].

After the deposition of cobalt nitrate and annealing at 350°C , the appearance of additional intense peaks corresponding to the Co_3O_4 phase are observed. The Raman spectrum of the ZnO/ Co_3O_4 heterostructure with a combination of individual ZnO and Co_3O_4 bands is shown in Figure 3b. Cobalt oxide (Co_3O_4) in the spinel phase has a cubic structure with the main Raman active modes at 185, 486, 532, and 687 cm^{-1} , which can be assigned to F_{2g} , E_g , F_{2g} , and A_{1g} phonons due to the octahedral (CoO_6) and tetrahedral (CO_4) symmetry [41,42]. The assignments of all observed peaks of ZnO and ZnO/ Co_3O_4 structures are presented in Table S1. The Raman spectra of the samples compared with the signal from the ITO glass substrate are shown in Figure S3 in the Supplementary Materials.

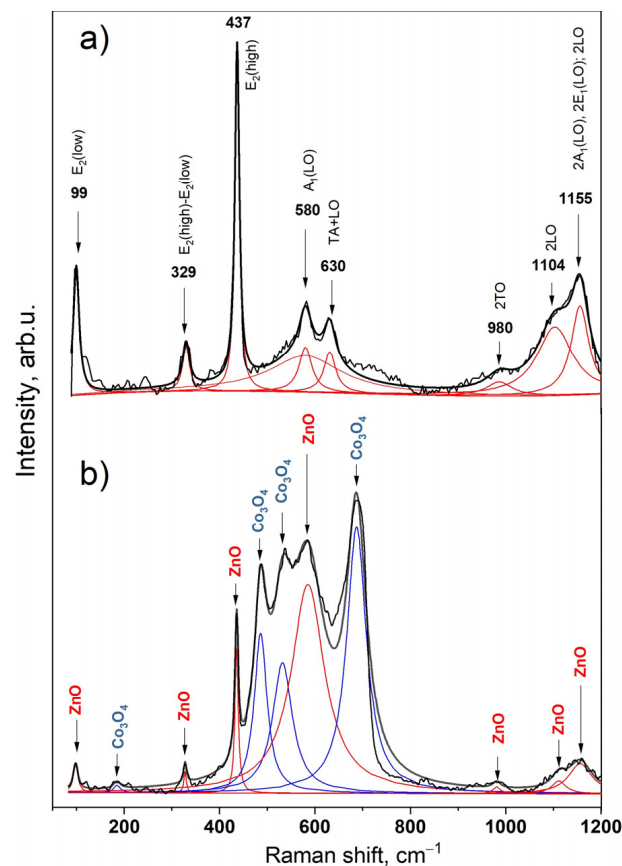


Figure 3. Raman spectra of (a) ZnO and (b) ZnO/Co₃O₄.

In addition, the presence of cobalt oxide was confirmed with energy-dispersive X-ray spectroscopy (EDS) analysis, the result of which is shown in Figure S2 for a pure ZnO sample. It is seen that there are no other elements except Zn and oxygen, and some low-intensity peaks corresponding to the substrate composition. The EDS result was able to confirm the presence of Co in the case of the ZnO/Co₃O₄ sample.

In order to evaluate information from the surface region of the material, XPS analysis was also employed. Comparing the total XPS spectrum of ZnO and ZnO/Co₃O₄, we can observe an additional peak related with the cobalt (Co) core levels (Figure 4a).

Characteristic XPS peaks of Zn 2p at the binding energies of 1021.9 and 1045 eV confirm the atomic states Zn²⁺ 2p_{3/2} and Zn²⁺ 2p_{1/2}, respectively. The Zn2p_{3/2} and Zn2p_{1/2} XPS peaks in the ZnO/Co₃O₄ samples are shifted upward in binding energy by 0.4 eV relative to the bare ZnO and have a larger half-width (Figure 4b).

These XPS Zn2p_{3/2} and Zn2p_{1/2} lines in the ZnO/Co₃O₄ samples can be represented as the sum of the XPS spectrum of the original ZnO and shifted to the right by 0.4 eV, with an intensity ratio of 1:4 (Figure 4c). The original spectrum belongs to ZnO atoms (Line A), in regions without Co₃O₄ particles. The spectrum shifted up in energy belongs to ZnO atoms, near which cobalt atoms are located (Line B).

Following the surface modification of ZnO with Co₃O₄, there was a noticeable shift of 0.5 eV toward higher binding energy in the O 1s peak as illustrated in Figure 4b. The O 1s peak can be divided into main peaks located at around 530 and 531 eV (Figure 4e). The presence of different metal cations can induce charge transfer effects leading to alterations in the electron density surrounding oxygen atoms and consequently influencing the position of the O 1s peak, as reported in references [43,44]. These findings suggest that the electronic cloud densities associated with surface Zn and O decrease as a result of some Co₃O₄ atoms bonding with them.

comes from the p–n junction regions at the interface of ZnO and Co₃O₄. When such regions are larger, the photocurrent is greater. A ZnO array layer of nanorods with a 25 mM concentration has poor p–n junction regions. As the length of the nanorods increases at the 50 mM concentration, the specific area for p–n junctions increases, and the maximum value of the photocurrent is achieved. With a further increase in the thickness of the nanorod array layer at the 75 mM concentration, the conditions for collecting photogenerated carriers worsen due to an increase in the path of carriers to the current substrate. In addition, increasing the length of nanorods leads to shadowing, so increasing the length beyond the optimal one will not lead to an increase in photocurrent.

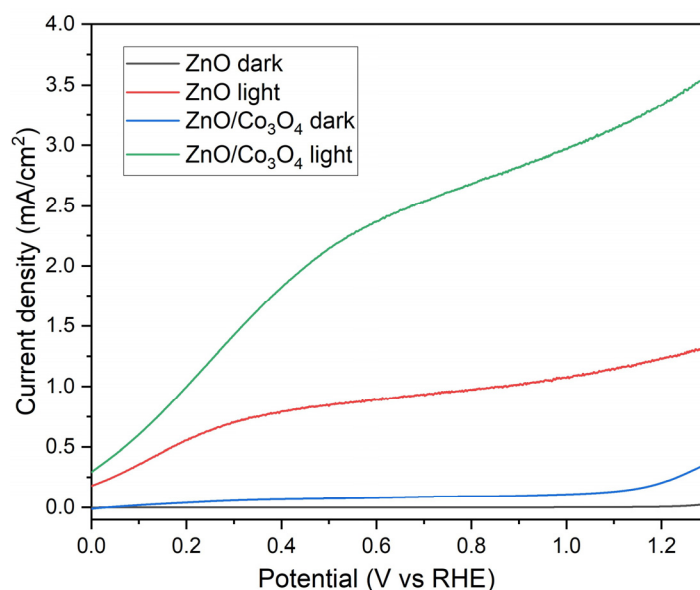


Figure 5. Comparison of LSV curves for bare ZnO nanorods and for ZnO/Co₃O₄ nanorods recorded at a scan rate of 10 mV/s in 0.5 M Na₂SO₃/Na₂S electrolyte.

After optimizing the bare ZnO nanorods, we deposited cobalt nitrate solution and annealed it at 350 °C to design the ZnO/Co₃O₄ material. In Figure 5, a comparison of linear sweep voltammetry between bare ZnO and ZnO/Co₃O₄ is presented. The current value is significantly higher in the case of ZnO/Co₃O₄, owing to the synergistic effects that enhance charge generation, separation, and transport, as discussed in [26,27]. The introduction of Co₃O₄ has notably boosted the photocurrent throughout the entire potential range. Notably, at 1.23 V, there is a significant difference of 3.46 mA/cm² between the dark and light current values, surpassing that of bare ZnO. This discrepancy underscores the synergistic effects and the improved electrochemical properties resulting from the incorporation of Co₃O₄.

We conducted a chronoamperometry experiment at 0.5 V, under chopped illumination, to compare the performance of ZnO/Co₃O₄ with that of pure ZnO. The photocurrent response was evaluated by alternately turning on and off simulated light, with each cycle lasting 20 s, as depicted in Figure 6a. ZnO/Co₃O₄ exhibits a much higher photocurrent than pristine ZnO. This aligns well with the findings from the LSV results. Chronoamperometries for the ZnO/Co₃O₄ electrodes obtained during 1300 s under chopped illumination are shown in Figure 6b. The *j*–*t* curve showing stability during 6000 s is shown in Figure S4. The current density initially drops to around 20%, but it subsequently displays an increasing trend compared to the initial value. This indicates the generation of new charge carriers and suggests that Co₃O₄ enhances the stability of the ZnO electrode. This observation further implies that the creation of a p–n junction within the ZnO/Co₃O₄ nanostructures effectively separates the photogenerated charge carriers, thereby reducing the recombination of photocatalytic charge carriers.

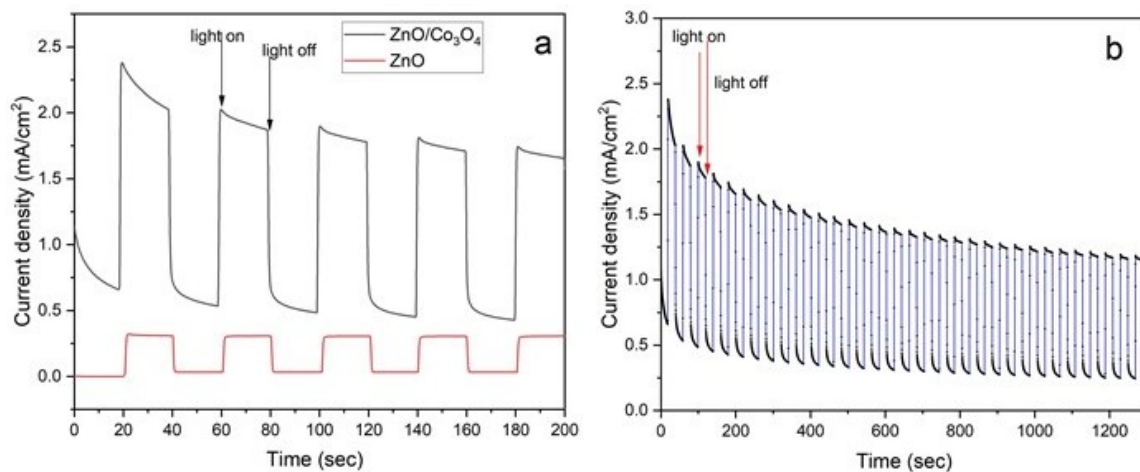


Figure 6. (a) Chronoamperometry I-t curves for the ZnO/Co₃O₄ compared with ZnO alone with an applied potential of 0.5 V versus RHE with 20 s light on/off cycles, and (b) ZnO/Co₃O₄ electrodes under chopped illumination (100 mW/cm²) during 1300 s in 0.5 M Na₂SO₃/Na₂S electrolyte.

To investigate electron transfer dynamics at the interface between the photoelectrode and the electrolyte, we utilized electrochemical impedance spectroscopy (EIS) as illustrated in Figure S5. The reduced radius of the Nyquist plot is observed in the case of ZnO/Co₃O₄ photoelectrodes, when compared to ZnO, indicating improved charge transport capabilities.

The conduction band energy positions of ZnO and Co₃O₄ are located at -0.5 eV and 0.35 eV, respectively. ZnO is an n-type semiconductor with a band gap of ~ 3.3 eV, and Co₃O₄ is a p-type semiconductor with a band gap of ~ 2.07 eV [47,48], as illustrated in Figure 7. When the ZnO/Co₃O₄ electrode is exposed to light, photogenerated electrons become excited, moving to the conduction band of ZnO, while holes are created in the VB of ZnO. Upon the contact of ZnO with Co₃O₄, there is a tendency for their Fermi levels to align, driven by the pursuit of equilibrium. This equilibration process involves the diffusion and drift of charge carriers between the two materials [49,50], resulting in the formation of a depletion layer at the interface. After equilibrium, the band diagram of Co₃O₄ is more shifted relative to ZnO; therefore, photogenerated electrons can move from Co₃O₄ to ZnO, while holes can move from the VB of ZnO to Co₃O₄ without any external bias potential (Figure 7).

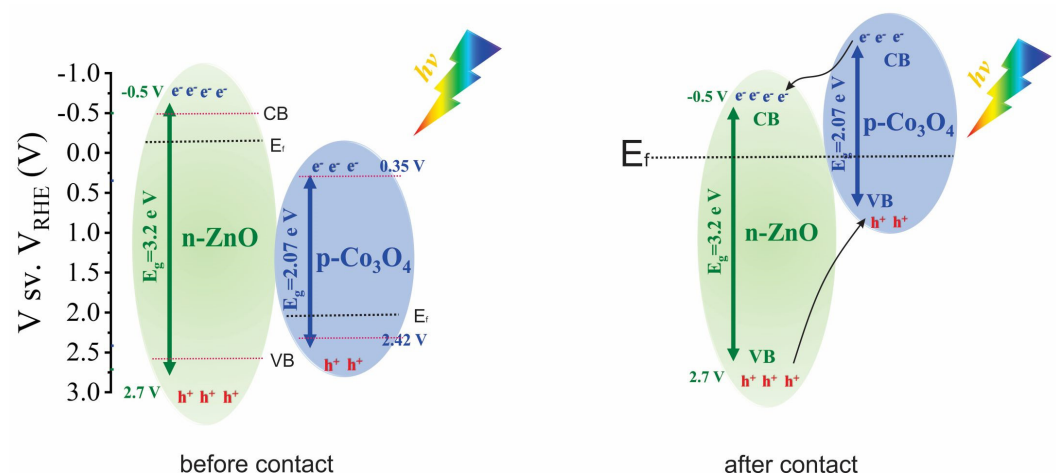


Figure 7. Schematic diagrams of energy bands of ZnO and Co₃O₄ and the charge separation process.

Under a positive applied bias potential, as is typically the case, electrons have the ability to migrate towards the platinum (Pt) cathode, where they engage in the reduction reaction of water, as depicted in Figure 8. As a result, holes drift within the valence band

(VB) and at the interface with the electrolyte. It is worth noting that in the case of bare ZnO, the process is primarily anodic photodecomposition rather than water oxidation.

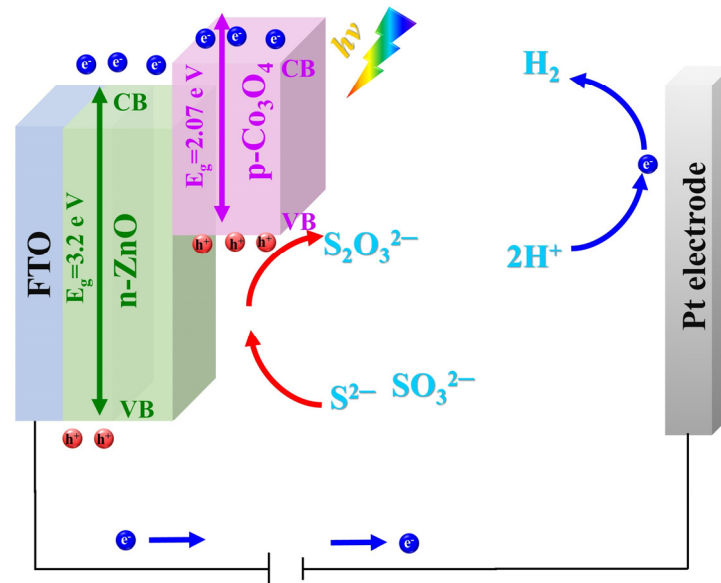


Figure 8. Schematic of the charge carrier's transfer in a PEC cell.

The $\text{Na}_2\text{S}+\text{Na}_2\text{SO}_3$ electrolyte is used as a sacrificial solution to reduce photocorrosion of the ZnO [51–53]. In this process, the S^{2-} ions from Na_2S can react with two holes in the VB of ZnO, forming S_2^{2-} . In addition, SO_3^{2-} ions act as hole scavengers preventing a back reaction by reducing S_2^{2-} to S^{2-} . These SO_3^{2-} ions can also react with S^{2-} to produce $\text{S}_2\text{O}_3^{2-}$. Consequently, the photogenerated holes oxidize $\text{Na}_2\text{S} + \text{Na}_2\text{SO}_3$ electrolyte rather than water. This also improves the photocatalytic activity of ZnO-based heterostructures [54].

The ZnO/ Co_3O_4 photocatalyst designed in our lab provides the highest photocurrent enhancement among some ZnO-based heterostructured photocatalysts with loading of other catalysts and other photocatalysts loaded with CoO_x as shown in Table 1.

Table 1. Comparison of ZnO and other metal oxides combined with metal oxide nanomaterials.

Metal Oxides	Electrolyte	Light Source	Photocurrent Enhancement at 1.23 V vs. RHE (Ma/Cm ²)	
ZnO/ Co_3O_4	0.5 M $\text{Na}_2\text{S}/\text{Na}_2\text{SO}_3$	Xe lamp 300 W	3.46	This work
ZnO/CoO	0.03 M borax	Xe lamp 300 W	1.26	[23]
ZnO/ WO_{3-x}	1 M Na_2SO_4	Xe arc lamp 300 W	2.39	[55]
ZnO NSs-NRs@ TiO_2 -Au	0.5 M Na_2SO_4	-	1.73	[56]
ZnO@ TiO_2	0.1 M NaOH	Xe lamp 450 W	0.40	[57]
$\text{SnS}_2/\text{b-ZnO}$	0.25 M $\text{Na}_2\text{S}/$ 0.35 M Na_2SO_3	Xe arc lamp 300 W	0.58	[58]
Y-ZnO	0.1 M Na_2SO_4	Xe arc lamp 500 W	0.50	[59]

The optical characteristics of samples were examined through UV-vis absorption spectroscopy. In Figure 9, the UV-vis absorption spectra of both the bare ZnO and ZnO/ Co_3O_4 heterostructures array are depicted. The photo of samples on the glass in the inset shows a transition from white to brown colors after cobalt deposition. The dominant absorption

occurs in the UV region, around ~ 380 nm, characteristic of ZnO. It is apparent that the absorption in the visible region increases after cobalt deposition.

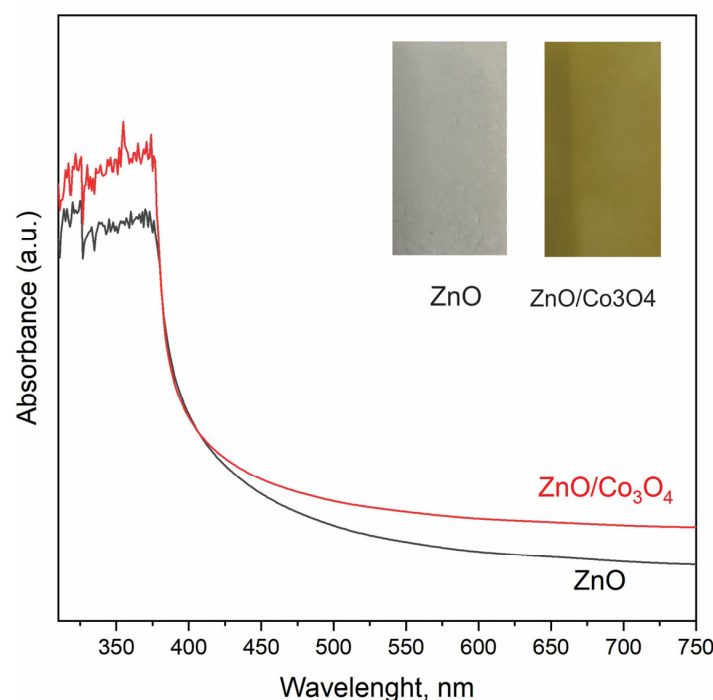


Figure 9. UV-vis absorption spectra of the bare ZnO and ZnO/Co₃O₄, the inset includes images of samples on the glass.

6. Conclusions

In conclusion, this research has demonstrated the successful utilization of a novel approach involving the combination of two different materials, namely ZnO nanorods as a photocatalyst and Co₃O₄ as a co-catalyst, achieved through chemical bath deposition (CBD) and a spin coating technique.

The solution concentration played a crucial role in the growth of zinc oxide nanorods, influencing their morphology, particularly the length of the nanorods. In this study, an optimal concentration of 50 mM was determined to be the best for efficient light absorption and enhancing photoelectrochemical properties.

Further improvement of PEC is realized by the formation of p–n junctions between ZnO and Co₃O₄ nanostructures. Notably, the photocurrent exhibited a significant value of 3.46 mA/cm² at 1.23 V for ZnO/Co₃O₄ composite, while bare ZnO demonstrated a photocurrent density of 0.8 mA/cm² at 1.23 V. These results underscore the potential of heterostructured photocatalysts as a promising area of research for the development of efficient photocatalysts and offer new insights into addressing the critical challenge of charge separation in water splitting.

Supplementary Materials: The following supporting information can be downloaded at: <https://www.mdpi.com/article/10.3390/ma17010146/s1>, Figure S1: SEM images of ZnO nanorods grown from a solution with a zinc concentration of (a) 25, (50), and 75 mM. The nanorod's diameter obtained from SEM image grown from a solution with a zinc concentration of 25mM, 50mM, and 75mM zinc precursor solution; Figure S2: (a) EDS analysis for bare ZnO and (b) ZnO/Co₃O₄; Figure S3: Raman spectra of ZnO (left) and ZnO/Co₃O₄ (right) samples along with Raman signal of ITO glass substrate; Figure S4: Comparison of LSV curves for bare ZnO nanorods with concentration of (a) 25, (b) 50 and 75 mM (c) recorded at scan rate of 10 mV/sec in 0.5 M Na₂SO₃/Na₂S electrolyte; Figure S5: Chronoamperometry j-t curves for the ZnO/Co₃O₄ at an applied potential of 0.5 V versus RHE during 6000 s; Figure S6: Nyquist plots for bare ZnO and (b) ZnO/Co₃O₄; Table S1: Raman modes of ZnO and Co₃O₄.

Author Contributions: Conceptualization, A.A.M., K.A.A. and Z.K.K.; data curation, A.A.M. and Z.K.K.; investigation, A.A.M., Z.K.K., R.N., A.S.A., A.T.T. and Y.Y.; methodology, A.A.M., R.N. and M.A.T.; supervision, A.A.M.; visualization, A.A.M., A.S.A., Y.Y. and A.T.T.; writing—original draft, A.A.M.; writing—review and editing, K.A.A. All authors have read and agreed to the published version of the manuscript.

Funding: This research was funded by Program of the Committee of Science of the Ministry Higher Education of the Republic of Kazakhstan, grant number no. AP09058501.

Informed Consent Statement: Not applicable.

Data Availability Statement: The data presented in this study are available upon request from the corresponding author.

Acknowledgments: A.A.M. thanks the Young Scientist Program of the Ministry of Science and Education of the Republic of Kazakhstan for financial support., grant number No. AP09058501 for 2021–2023. A.A.M. greatly acknowledge technical supported from Nazarbayev University.

Conflicts of Interest: The authors declare no conflicts of interest.

References

1. Zhao, Y.; Niu, Z.; Zhao, J.; Xue, L.; Fu, X.; Long, J. Recent advancements in photoelectrochemical water splitting for hydrogen production. *Electrochem. Energy Rev.* **2023**, *6*, 14. [[CrossRef](#)]
2. Bozheyev, F. Transition metal dichalcogenide thin films for solar hydrogen production. *Curr. Opin. Electrochem.* **2022**, *34*, 100995. [[CrossRef](#)]
3. Bozheyev, F.; Ellmer, K. Thin film transition metal dichalcogenide photoelectrodes for solar hydrogen evolution: A review. *J. Mater. Chem. A* **2022**, *10*, 9327–9347. [[CrossRef](#)]
4. Bozheyev, F.; Akinoglu, E.M.; Wu, L.; Lu, H.; Nemkayeva, R.; Xue, Y.; Jin, M.; Giersig, M. Band gap optimization of tin tungstate thin films for solar water oxidation. *Int. J. Hydrogen Energy* **2020**, *45*, 8676–8685. [[CrossRef](#)]
5. Mussabek, G.; Zhylkybayeva, N.; Baktygeray, S.; Yermukhamed, D.; Taurbayev, Y.; Sadykov, G.; Zaderko, A.N.; Lisnyak, V.V. Preparation and characterization of hybrid nanopowder based on nanosilicon decorated with carbon nanostructures. *Appl. Nanosci.* **2022**, *13*, 6709–6718. [[CrossRef](#)]
6. Ravi, P.; Rao, V.N.; Shankar, M.; Sathish, M. CuOCr₂O₃ core-shell structured co-catalysts on TiO₂ for efficient photocatalytic water splitting using direct solar light. *Int. J. Hydrogen Energy* **2018**, *43*, 3976–3987. [[CrossRef](#)]
7. Tiwari, A.; Duvva, N.; Rao, V.N.; Venkatakrishnan, S.M.; Giribabu, L.; Pal, U. Tetrathiafulvalene scaffold-based sensitizer on hierarchical porous TiO₂: Efficient light-harvesting material for hydrogen production. *J. Phys. Chem. C* **2018**, *123*, 70–81. [[CrossRef](#)]
8. Xie, X.; Wang, R.; Ma, Y.; Chen, J.; Cui, Q.; Shi, Z.; Li, Z.; Xu, C. Photothermal-effect-enhanced photoelectrochemical water splitting in MXene-nanosheet-modified ZnO nanorod arrays. *ACS Appl. Nano Mater.* **2022**, *5*, 11150–11159. [[CrossRef](#)]
9. Liccardo, L.; Lushaj, E.; Dal Compare, L.; Moretti, E.; Vomiero, A. Nanoscale ZnO/ α -Fe₂O₃ Heterostructures: Toward Efficient and Low-Cost Photoanodes for Water Splitting. *Small Sci.* **2022**, *2*, 2100104. [[CrossRef](#)]
10. Abdullin, K.A.; Gabdullin, M.T.; Gritsenko, L.; Ismailov, D.V.; Kalkozova, Z.K.; Kumekov, S.; Mukash, Z.O.; Sazonov, A.Y.; Terukov, E. Electrical, optical, and photoluminescence properties of ZnO films subjected to thermal annealing and treatment in hydrogen plasma. *Semiconductors* **2016**, *50*, 1010–1014. [[CrossRef](#)]
11. Abdullin, K.A.; Gritsenko, L.; Kumekov, S.; Markhabaeva, A.; Terukov, E. Effect of heat and plasma treatments on the photoluminescence of zinc-oxide films. *Semiconductors* **2018**, *52*, 177–183. [[CrossRef](#)]
12. Kedruk, Y.; Baigarinova, G.; Gritsenko, L.; Cicero, G.; Abdullin, K.A. Facile Low-Cost Synthesis of Highly Photocatalytically Active Zinc Oxide Powders. *Front. Mater.* **2022**, *9*, 869493. [[CrossRef](#)]
13. Rehman, S.; Ullah, R.; Butt, A.; Gohar, N. Strategies of making TiO₂ and ZnO visible light active. *J. Hazard. Mater.* **2009**, *170*, 560–569. [[CrossRef](#)] [[PubMed](#)]
14. Prikhodko, O.Y.; Aitzhanov, M.; Gusseinov, N.; Kalkozova, Z.K.; Dikhanbaev, K.; Markhabayeva, A.; Myrzabekova, M.; Nemkayeva, R.; Mukhametkarimov, Y.S. Photocatalytic activity of liquid-phase exfoliated gallium selenide flakes. *Chalcogenide Lett.* **2021**, *18*, 777–781. [[CrossRef](#)]
15. Sakthivel, S.; Neppolian, B.; Shankar, M.; Arabindoo, B.; Palanichamy, M.; Murugesan, V. Solar photocatalytic degradation of azo dye: Comparison of photocatalytic efficiency of ZnO and TiO₂. *Sol. Energy Mater. Sol. Cells* **2003**, *77*, 65–82. [[CrossRef](#)]
16. Chen, C.-C. Degradation pathways of ethyl violet by photocatalytic reaction with ZnO dispersions. *J. Mol. Catal. A Chem.* **2007**, *264*, 82–92. [[CrossRef](#)]
17. Kansal, S.; Singh, M.; Sud, D. Studies on photodegradation of two commercial dyes in aqueous phase using different photocatalysts. *J. Hazard. Mater.* **2007**, *141*, 581–590. [[CrossRef](#)]
18. Rahman, Q.I.; Ahmad, M.; Misra, S.K.; Lohani, M.B. Hexagonal ZnO nanorods assembled flowers for photocatalytic dye degradation: Growth, structural and optical properties. *Superlattices Microstruct.* **2013**, *64*, 495–506. [[CrossRef](#)]

19. Harathi, N.; Bollu, M.; Pasupuleti, K.S.; Tauanov, Z.; Peta, K.R.; Kim, M.-D.; Reddeppa, M.; Sarkar, A.; Rao, V.N. PrGO decorated TiO₂ nanoplates hybrid nanocomposite for augmented NO₂ gas detection with faster gas kinetics under UV light irradiation. *Sens. Actuators B Chem.* **2022**, *358*, 131503. [[CrossRef](#)]
20. Shahzad, S.; Javed, S.; Usman, M. A review on synthesis and optoelectronic applications of nanostructured ZnO. *Front. Mater.* **2021**, *8*, 613825. [[CrossRef](#)]
21. Redkin, A.N.; Yakimov, E.E.; Evstafieva, M.V.; Yakimov, E.B. Grown and characterization of ZnO aligned nanorod arrays for sensor applications. *Energies* **2021**, *14*, 3750. [[CrossRef](#)]
22. A Barzinji, A. Synthesis, properties and uses of ZnO nanorods: A mini review. *Int. Nano Lett.* **2021**, *12*, 153–168.
23. Nandanapalli, K.R.; Mudusu, D.; Yu, J.-S.; Lee, S. Stable and sustainable photoanodes using zinc oxide and cobalt oxide chemically gradient nanostructures for water-splitting applications. *J. Colloid Interface Sci.* **2020**, *558*, 9–20. [[CrossRef](#)]
24. Tahira, A.; Ibupoto, Z.H.; Nafady, A.; Willander, M.; Nur, O. Efficient and Stable Co₃O₄/ZnO Nanocomposite for Photochemical Water Splitting. *J. Clust. Sci.* **2021**, *33*, 387–394. [[CrossRef](#)]
25. Tien, T.-M.; Chen, E.L. A Novel ZnO/Co₃O₄ Nanoparticle for Enhanced Photocatalytic Hydrogen Evolution under Visible Light Irradiation. *Catalysts* **2023**, *13*, 852. [[CrossRef](#)]
26. Yang, Y.; Cheng, W.; Cheng, Y.F. Preparation of Co₃O₄@ZnO core-shell nanocomposites with intrinsic pn junction as high-performance photoelectrodes for photoelectrochemical cathodic protection under visible light. *Appl. Surf. Sci.* **2019**, *476*, 815–821. [[CrossRef](#)]
27. Zhang, L.; Li, H.; Yang, B.; Zhou, Y.; Zhang, Z.; Wang, Y. Photo-deposition of ZnO/Co₃O₄ core-shell nanorods with pn junction for efficient oxygen evolution reaction. *J. Solid State Electrochem.* **2019**, *23*, 3287–3297. [[CrossRef](#)]
28. Abdullin, K.A.; Zhmagulov, S.; Ismailova, G.; Kalkozova, Z.K.; Kudryashov, V.; Serikkanov, A. Synthesis of Heterogeneous ZnO/Co₃O₄ Nanostructures by Chemical Deposition from Solutions. *Tech. Phys.* **2020**, *65*, 1139–1143. [[CrossRef](#)]
29. Xi, F.; Bozheyev, F.; Han, X.; Rusu, M.; Rappich, J.; Abdi, F.F.; Bogdanoff, P.; Kaltsoyannis, N.; Fiechter, S. Enhancing Hydrogen Evolution Reaction via Synergistic Interaction between the [Mo₃S₁₃] 2-Cluster Co-Catalyst and WSe₂ Photocathode. *ACS Appl. Mater. Interfaces* **2022**, *14*, 52815–52824. [[CrossRef](#)]
30. Markhabayeva, A.A.; Moniruddin, M.; Dupre, R.; Abdullin, K.A.; Nuraje, N. Designing of WO₃@Co₃O₄ heterostructures to enhance photoelectrochemical performances. *J. Phys. Chem. A* **2019**, *124*, 486–491. [[CrossRef](#)]
31. McPeak, K.M.; Le, T.P.; Britton, N.G.; Nickolov, Z.S.; Elabd, Y.A.; Baxter, J.B. Chemical bath deposition of ZnO nanowires at near-neutral pH conditions without hexamethylenetetramine (HMTA): Understanding the role of HMTA in ZnO nanowire growth. *Langmuir* **2011**, *27*, 3672–3677. [[CrossRef](#)] [[PubMed](#)]
32. Ashfold, M.N.; Doherty, R.P.; Ndifor-Angwafor, N.G.; Riley, D.J.; Sun, Y. The kinetics of the hydrothermal growth of ZnO nanostructures. *Thin Solid Film.* **2007**, *515*, 8679–8683. [[CrossRef](#)]
33. Kaphle, A.; Reed, T.; Apblett, A.; Hari, P. Doping efficiency in cobalt-doped ZnO nanostructured materials. *J. Nanomater.* **2019**, *2019*, 7034620. [[CrossRef](#)]
34. Kalita, A.; Kalita, M.P. Effects of size reduction on microstructural, optical, vibrational, magnetic and photocatalytic properties of ZnO nanocrystals. *Mater. Charact.* **2018**, *137*, 109–118. [[CrossRef](#)]
35. Abdullin, K.A.; Gabdullin, M.T.; Zhmagulov, S.K.; Ismailova, G.A.; Gritsenko, L.V.; Kedruk, Y.Y.; Mirzaeian, M. Stabilization of the surface of ZnO films and elimination of the aging effect. *Materials* **2021**, *14*, 6535. [[CrossRef](#)] [[PubMed](#)]
36. Kaningini, A.G.; Azizi, S.; Sintwa, N.; Mokalane, K.; Mohale, K.C.; Mudau, F.N.; Maaza, M. Effect of Optimized Precursor Concentration, Temperature, and Doping on Optical Properties of ZnO Nanoparticles Synthesized via a Green Route Using Bush Tea (*Athrixia phylicoides* DC.) Leaf Extracts. *ACS Omega* **2022**, *7*, 31658–31666. [[CrossRef](#)]
37. Lestari, A.; Iwan, S.; Djuhana, D.; Imawan, C.; Harmoko, A.; Fauzia, V. Effect of precursor concentration on the structural and optical properties of ZnO nanorods prepared by hydrothermal method. In *AIP Conference Proceedings*; AIP Publishing LLC: Melville, NY, USA, 2016; p. 020027.
38. Horachit, C.; Moonnoi, S.; Ruankham, P.; Choopun, S.; Intaniwet, A. Effects of precursor concentration on hydrothermally grown ZnO nanorods as electron transporting layer in perovskite solar cells. *Mater. Today Proc.* **2019**, *17*, 1217–1223. [[CrossRef](#)]
39. Cuscó, R.; Alarcón-Lladó, E.; Ibáñez, J.; Artús, L.; Jiménez, J.; Wang, B.; Callahan, M.J. Temperature dependence of Raman scattering in ZnO. *Phys. Rev. B* **2007**, *75*, 165202. [[CrossRef](#)]
40. Kuryliszyn-Kudelska, I.; Hadžić, B.; Sibera, D.; Romčević, M.; Romčević, N.; Narkiewicz, U.; Łojkowski, W.; Arciszewska, M.; Dobrowolski, W. Magnetic properties of ZnO(Co) nanocrystals. *J. Alloys Compd.* **2013**, *561*, 247–251. [[CrossRef](#)]
41. Diallo, A.; Beye, A.; Doyle, T.B.; Park, E.; Maaza, M. Green synthesis of Co₃O₄ nanoparticles via *Aspalathus linearis*: Physical properties. *Green Chem. Lett. Rev.* **2015**, *8*, 30–36. [[CrossRef](#)]
42. Tortosa, M.; Manjón, F.; Mollar, M.; Marí, B. ZnO-based spinels grown by electrodeposition. *J. Phys. Chem. Solids* **2012**, *73*, 1111–1115. [[CrossRef](#)]
43. Pawlak, D.A.; Ito, M.; Oku, M.; Shimamura, K.; Fukuda, T. Interpretation of XPS O (1s) in mixed oxides proved on mixed perovskite crystals. *J. Phys. Chem. B* **2002**, *106*, 504–507. [[CrossRef](#)]
44. Li, M.; Meng, G.; Huang, Q.; Zhang, S. Improved sensitivity of polychlorinated-biphenyl-orientated porous-ZnO surface photovoltage sensors from chemisorption-formed ZnO-CuPc composites. *Sci. Rep.* **2014**, *4*, 4284. [[CrossRef](#)] [[PubMed](#)]

45. Arya, S.; Mahajan, P.; Mahajan, S.; Khosla, A.; Datt, R.; Gupta, V.; Young, S.-J.; Oruganti, S.K. influence of processing parameters to control morphology and optical properties of Sol-Gel synthesized ZnO nanoparticles. *ECS J. Solid State Sci. Technol.* **2021**, *10*, 023002. [[CrossRef](#)]
46. Benrezgua, E.; Deghfel, B.; Zoukel, A.; Basirun, W.J.; Amari, R.; Boukhari, A.; Yaakob, M.K.; Kheawhom, S.; Mohamad, A.A. Synthesis and properties of copper doped zinc oxide thin films by sol-gel, spin coating and dipping: A characterization review. *J. Mol. Struct.* **2022**, *1267*, 133639. [[CrossRef](#)]
47. Gong, H.; Cao, Y.; Zhang, Y.; Zhang, Y.; Liu, K.; Cao, H.; Yan, H. The synergetic effect of dual co-catalysts on the photocatalytic activity of square-like WO₃ with different exposed facets. *RSC Adv.* **2017**, *7*, 19019–19025. [[CrossRef](#)]
48. Ivanishcheva, A.P.; Sysoev, V.V.; Abdullin, K.A.; Nesterenko, A.V.; Khubezhov, S.A.; Petrov, V.V. The Application of Combined Visible and Ultraviolet Irradiation to Improve the Functional Characteristics of Gas Sensors Based on ZnO/SnO₂ and ZnO/Au Nanorods. *Chemosensors* **2023**, *11*, 200. [[CrossRef](#)]
49. Chakraborty, A.K.; Akter, M.S.; Haque, M.A.; Khan, G.A.; Alam, M.S. Synthesis of Co₃O₄/WO₃ nanoheterojunction photocatalyst for the decomposition of organic pollutants under visible light irradiation. *J. Clust. Sci.* **2013**, *24*, 701–713. [[CrossRef](#)]
50. Zhao, X.; Ji, H.; Jia, Q.; Wang, M. A nanoscale Co₃O₄-WO₃ p-n junction sensor with enhanced acetone responsivity. *J. Mater. Sci. Mater. Electron.* **2015**, *26*, 8217–8223. [[CrossRef](#)]
51. Prabhu, Y.T.; Rao, V.N.; Shankar, M.V.; Sreedhar, B.; Pal, U. The facile hydrothermal synthesis of CuO@ZnO heterojunction nanostructures for enhanced photocatalytic hydrogen evolution. *New J. Chem.* **2019**, *43*, 6794–6805. [[CrossRef](#)]
52. Govatsi, K.; Antonelou, A.; Sygellou, L.; Neophytides, S.G.; Yannopoulos, S.N. Hybrid ZnO/MoS₂ Core/Sheath Heterostructures for Photoelectrochemical Water Splitting. *Appl. Nano* **2021**, *2*, 148–161. [[CrossRef](#)]
53. Kim, H.; Yong, K. Highly efficient photoelectrochemical hydrogen generation using a quantum dot coupled hierarchical ZnO nanowires array. *ACS Appl. Mater. Interfaces* **2013**, *5*, 13258–13264. [[CrossRef](#)] [[PubMed](#)]
54. Sánchez-Tovar, R.; Fernández-Domene, R.M.; Montañés, M.; Sanz-Marco, A.; Garcia-Anton, J. ZnO/ZnS heterostructures for hydrogen production by photoelectrochemical water splitting. *RSC Adv.* **2016**, *6*, 30425–30435. [[CrossRef](#)]
55. Chen, Y.; Wang, L.; Gao, R.; Zhang, Y.-C.; Pan, L.; Huang, C.; Liu, K.; Chang, X.-Y.; Zhang, X.; Zou, J.-J. Polarization-Enhanced direct Z-scheme ZnO-WO_{3-x} nanorod arrays for efficient piezoelectric-photoelectrochemical Water splitting. *Appl. Catal. B Environ.* **2019**, *259*, 118079. [[CrossRef](#)]
56. Cai, J.; Cao, J.; Tao, H.; Li, R.; Huang, M. Three-dimensional ZnO@TiO₂ core-shell nanostructures decorated with plasmonic Au nanoparticles for promoting photoelectrochemical water splitting. *Int. J. Hydrogen Energy* **2021**, *46*, 36201–36209. [[CrossRef](#)]
57. Hernández, S.; Cauda, V.; Chiodoni, A.; Dallorto, S.; Sacco, A.; Hidalgo, D.; Celasco, E.; Pirri, C.F. Optimization of 1D ZnO@TiO₂ core-shell nanostructures for enhanced photoelectrochemical water splitting under solar light illumination. *ACS Appl. Mater. Interfaces* **2014**, *6*, 12153–12167. [[CrossRef](#)]
58. Bagal, I.V.; Jun, S.; Choi, M.; Abdullah, A.; Waseem, A.; Ahn, S.; Kulkarni, M.A.; Cho, Y.-H.; Ryu, S.-W. Investigation of charge carrier dynamics in beaded ZnO nanowire decorated with SnS₂/IrO_x cocatalysts for enhanced photoelectrochemical water splitting. *Appl. Surf. Sci.* **2023**, *613*, 156091. [[CrossRef](#)]
59. Wei, Y.; Wang, L.; Chen, C. Yttrium doping enhances the photoelectrochemical water splitting performance of ZnO nanorod array films. *J. Alloys Compd.* **2022**, *896*, 163144. [[CrossRef](#)]

Disclaimer/Publisher's Note: The statements, opinions and data contained in all publications are solely those of the individual author(s) and contributor(s) and not of MDPI and/or the editor(s). MDPI and/or the editor(s) disclaim responsibility for any injury to people or property resulting from any ideas, methods, instructions or products referred to in the content.